Earth and Planetary Science Letters 474 (2017) 334–344

Contents lists available at ScienceDirect

Earth and Planetary Science Letters

www.elsevier.com/locate/epsl

Highly variable coastal deformation in the 2016 M_W7.8 Kaikōura earthquake reflects rupture complexity along a transpressional plate boundary

K.J. Clark [a,*], E.K. Nissen [b], J.D. Howarth [a,1], I.J. Hamling [a], J.J. Mountjoy [c], W.F. Ries [a], K. Jones [a], S. Goldstien [d], U.A. Cochran [a], P. Villamor [a], S. Hreinsdóttir [a], N.J. Litchfield [a], C. Mueller [a], K.R. Berryman [a], D.T. Strong [a]

[a] GNS Science, PO Box 30 368, Lower Hutt 5040, New Zealand
[b] School of Earth and Ocean Sciences, University of Victoria, 3800 Finnerty Road, Victoria B.C., V8P 5C2, Canada
[c] National Institute of Water and Atmospheric Research, Private Bag 14901, Wellington 6241, New Zealand
[d] School of Biological Sciences, University of Canterbury, Private Bag 4800, Christchurch, New Zealand

ARTICLE INFO

Article history:
Received 1 April 2017
Received in revised form 25 June 2017
Accepted 27 June 2017
Available online 20 July 2017
Editor: A. Yin

Keywords:
coastal deformation
multi-fault rupture
Kaikōura earthquake
lidar differencing
plate boundary

ABSTRACT

Coseismic coastal deformation is often used to understand slip on offshore faults in large earthquakes but in the 2016 M_W7.8 Kaikōura earthquake multiple faults ruptured across and sub-parallel to the coastline. Along ∼110 km of coastline, a rich dataset of coastal deformation comprising airborne lidar differencing, field surveying and satellite geodesy reveals highly variable vertical displacements, ranging from −2.5 to 6.5 m. These inform a refined slip model for the Kaikōura earthquake which incorporates changes to the slip on offshore faults and inclusion of an offshore reverse crustal fault that accounts for broad, low-amplitude uplift centered on Kaikōura Peninsula. The exceptional detail afforded by differential lidar and the high variability in coastal deformation combine to form the highest-resolution and most complex record of coseismic coastal deformation yet documented. This should prompt reassessment of coastal paleoseismic records that may not have considered multi-fault ruptures and high complexity deformation fields.

© 2017 The Authors. Published by Elsevier B.V. This is an open access article under the CC BY-NC-ND license (http://creativecommons.org/licenses/by-nc-nd/4.0/).

1. Introduction

Sudden coastal uplift and its direct association with earthquakes was first documented by FitzRoy and Darwin in south-central Chile in 1835 (FitzRoy, 1839) and since the 1960s, measurements of coseismic coastal uplift and subsidence have been used to understand the location and geometry of the fault source, slip distribution and segmentation of many earthquakes (e.g. Awata et al., 2008; Briggs et al., 2006; Hayes et al., 2010; Plafker, 1969; Taylor et al., 2008). Observations of coseismic coastal uplift also underpin the use of uplifted coastal geomorphology for determining the timing and magnitude of paleoearthquakes on offshore faults (e.g. Berryman et al., 2011; Rockwell et al., 2016; Shaw et al., 2008). Paleoseismic applications of coastal uplift are typically predicated on simple assumptions of single planar fault ruptures and do little to account for rupture complexity. Well documented records of coastal uplift during earthquakes, especially complex ruptures, provide an important context for evaluating the assumptions that underpin coastal paleoseismic studies.

Extensive coastal uplift was one of the more apparent impacts of the 2016 M_W7.8 Kaikōura earthquake, which is one of the most complex earthquakes ever observed with instrumentation (Hamling et al., 2017) (Figs. 1 and 2). There remain ambiguities in the slip model for this event that are not yet resolved despite it being well captured by seismological and geodetic instrumentation, and satellite interferometric synthetic aperture radar (InSAR) measurements of ground deformation (Hamling et al., 2017; Kaiser et al., 2017). Rupture of an underlying low-angle thrust fault or the subduction interface is generally required to fit teleseismic observations (Duputel and Rivera, 2017; Hollingsworth et al., 2017), and modeling of two sizable regions of seafloor deformation (one consistent with a subduction interface source) produce the best-fit to tsunami tide gauge data (Bai et al., 2017). Yet, geodetic and InSAR measurements, consistent with field observations of extensive and large (up to 12 m) fault surface ruptures,

* Corresponding author.
E-mail address: K.Clark@gns.cri.nz (K.J. Clark).
[1] Now at: School of Geography, Environment and Earth Sciences, Victoria University of Wellington, PO Box 600, Wellington 6140, New Zealand.

http://dx.doi.org/10.1016/j.epsl.2017.06.048
0012-821X/© 2017 The Authors. Published by Elsevier B.V. This is an open access article under the CC BY-NC-ND license (http://creativecommons.org/licenses/by-nc-nd/4.0/).

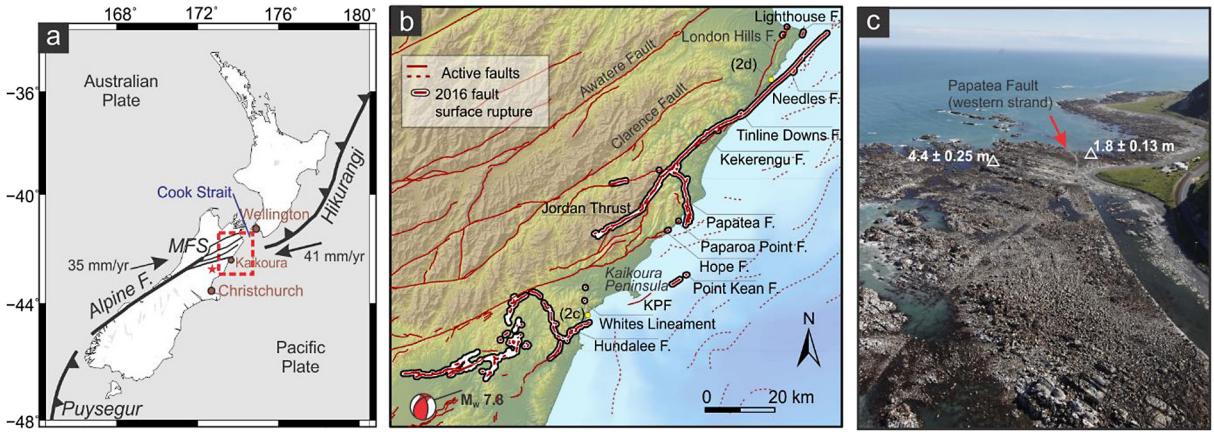

Fig. 1. Tectonic setting, surface ruptures and uplifted coastline of the 2016 M_W7.8 Kaikōura earthquake. (a) Plate tectonic setting of the Kaikōura earthquake, MFS: Marlborough fault system, plate motion rates from Wallace et al. (2012). (b) Fault surface ruptures of the Kaikōura earthquake (Litchfield et al., 2017) and active faults of the region (onshore faults from Langridge et al., 2016, offshore faults courtesy of NIWA, KPF: Kaikoura Peninsula fault as inferred by Barrell, 2015); only fault ruptures near the coast and offshore are labeled. (2c) and (2d) denotes the location of the photos shown in Fig. 2c and 2d. (c) The coastal trace of the western strand of the Papatea fault (red arrow) at Waipapa Bay. White triangles show the location of field measurements of coastal uplift. Photo view direction is southward, photo credit: Steve Lawson. (For interpretation of the references to color in this figure legend, the reader is referred to the web version of this article.)

Fig. 2. Examples of coastal uplift due to the M_w 7.8 Kaikōura earthquake. (a) Uplifted coastal platform between the two strands of the Papatea fault (see location in Fig. 3c), the brown algae formerly inhabited the subtidal zone, vertical displacement here was 4.4 ± 0.25 m. (b) Detail of the decaying holdfast of bull kelp (*Durvillaea antarctica*). (c) Uplifted coastline near Goose Bay, here the distinctive horizontal white band of bleached coralline algae marks the former mean low water mark; vertical displacement here was 1.5 ± 0.27 m. Photo location is marked in Fig. 1b. (d) Coastal uplift north of the Waima River, vertical displacement here was 2.9 ± 0.34 m. Photo location is marked in Fig. 1b.

indicate crustal faulting dominated the seismic moment release (Hamling et al., 2017). Resolving the involvement of the subduction interface and the extent of offshore fault rupture in the Kaikoura earthquake has implications for future seismic and tsunami hazard on the southern Hikurangi plate boundary, and for understanding earthquake hazards at analogous transpressional plate boundaries globally.

In this study we present a high-resolution record of coseismic coastal deformation that contributes to the understanding of slip on faults that cross the coastline, provides insights into offshore fault ruptures, and offers context for re-evaluating paleoseismic studies using coastal deformation as a primary dataset. We collected post-earthquake field measurements of coastal uplift using displaced low-tidal biota, and mapped coseismic vertical change

using pre- and post-earthquake airborne lidar surveys that cover 70% of the deformed coastline. Post-earthquake mapping of the fresh rupture scarp along the offshore Needles fault reveals submarine coseismic vertical offsets, which can be integrated with onshore vertical coastal deformation to constrain slip. Lidar differencing, along with closely-spaced field surveys, capture unprecedented detail of the coastal deformation associated with a complex earthquake on a transpressional plate boundary.

2. Background

The 14 November 2016 M_w7.8 Kaikōura earthquake occurred in the north-eastern South Island of New Zealand at the boundary between the Australian and Pacific tectonic plates (Fig. 1a). The north-eastern Marlborough region represents a transition zone from oblique continental collision in the south along the Alpine fault to subduction in the north along the Hikurangi subduction zone (Wallace et al., 2012). The Marlborough Fault System consists of a series of dextral strike-slip faults that accommodate at least 80% of Australia/Pacific Plate motion in the northern South Island, and it is possible that they may link at depth with the far southern part of the Hikurangi subduction zone (Wallace et al., 2012). Immediately to the south in North Canterbury the faults are predominantly reverse and transpressional, with much lower slip rates (Litchfield et al., 2014) (Fig. 1b). Pleistocene marine terraces provide long-term uplift rates ranging from ∼1.1 mm/yr to 0.5 mm/yr along the Kaikōura coastline (Ota et al., 1996) while Holocene marine terraces, although observed along the same coastline, have only been documented at Kaikōura Peninsula where there have been at least 3 uplift events in the past 3000 years (Barrell, 2015).

The Kaikōura earthquake initiated near Waiau in North Canterbury at 12:03 am local time at a depth of 15 km with an oblique thrust mechanism; the rupture propagated south–west to north–east over ∼2 min and terminated offshore in Cook Strait (Kaiser et al., 2017) (Fig. 1a). Meter-scale surface rupture occurred on at least fourteen faults, including >10 m dextral displacements on the Kekerengu fault (Litchfield et al., 2017), and a tsunami with runup of up to 7 m was generated (Power et al., 2017).

In historic and recent large earthquakes, coseismic coastal deformation has been measured by a variety of methods, with the diversity of techniques, accuracy and spatial density of measurements generally increasing over time. A common feature of most studies of coseismic coastal uplift is the use of displaced intertidal biozones to measure uplift. In tropical regions, coral microatolls are particularly sensitive recorders of tide levels (e.g. Briggs et al., 2006; Meltzner et al., 2006; Taylor et al., 2008) while in temperate regions coralline algae, macroalgae and sessile molluscs are used (e.g. Awata et al., 2008; Bodin and Klinger, 1986; Jaramillo et al., 2017; Melnick et al., 2012a; Plafker, 1969). GPS observations are a source of precise point measurements of uplift (Konca et al., 2007; Subarya et al., 2006) while satellite imagery and InSAR can provide more complete spatial coverage (Hayes et al., 2010; Meltzner et al., 2006; Subarya et al., 2006). Following the 2010 M_W8.8 Maule earthquake (Melnick et al., 2012a) measured uplift by comparing a pre-earthquake lidar with post-earthquake differential GPS tracks, which appears to be the first record of using lidar to detect coseismic coastal change. However, the availability of extensive lidar coverage from both before *and* after the Kaikōura earthquake is unparalleled for a major coastal rupture.

3. Methods

3.1. Field measurements

Coseismic coastal uplift was measured in the field at 39 sites using the post-earthquake elevation of algae that, prior to the earthquake, lived up to and around mean low water (MLW) elevation (Fig. 2). The upper limit of bull kelp (*Durvillaea antarctica*) and the associated band of coralline algae was used at shore lines experiencing high wave energy, whereas the upper limit of *Carpophyllum maschalocarpum* and associated coralline algae was used in areas of lower wave energy. Surveying was undertaken using a level, tripod and staff to obtain the difference in height between the MLW markers and the tide level at the time of surveying. Tide level at the time of surveying was then corrected relative to mean sea level. The survey points were not put into a global positioning projection or vertical datum as all local geodetic benchmarks had moved in the earthquake. The number of survey points collected at each site ranged from 1–21 (mean = 11). Surveying commenced five days after the earthquake and all points (except Lake Grassmere) were collected within 2.5 weeks of the earthquake. Further details on the methodology of using biological markers to measure coastal deformation can be found in Supplementary Material A. The uncertainty on mean uplift measurements from each site is reported as a 95% confidence interval estimated from propagation of the systematic and statistical uncertainties by summation in quadrature (Supplementary Material A, Text A1).

3.2. Lidar differencing

The Kaikōura coastline was surveyed with airborne lidar in July 2012 and on 19th–21st November 2016 (details of lidar acquisition are in Supplementary Material A, Text A2), resulting in a ∼0.5–4 km-wide, ∼90 km-long coastal strip of repeat, sub-meter resolution topography that extends from ∼4.5 years before to ∼1 week after the Kaikōura earthquake (Fig. 3a). There were no significant earthquakes in the area of joint coverage before the Kaikōura mainshock and the largest regional events, the 2013 Cook Strait sequence (M_w5.7, 5.8 and 6.6), produced <5 mm of vertical deformation in the Kaikōura region (Hamling et al., 2014). Over wavelengths of hundreds of meters, differences between the two "bare earth" (classified ground return) datasets therefore reflect coseismic and earliest post-seismic deformation of the 2016 Kaikōura earthquake. At shorter wavelengths, the paired lidar surveys also capture erosional and depositional processes, including landslides and rockfalls triggered by the Kaikōura earthquake.

To investigate vertical deformation across the area of joint lidar coverage, we subtract a 1 m-pixel 2012 lidar digital terrain model (DTM) from the equivalent 2016 DTM. In neglecting lateral motions of up to several meters in the earthquake, this subtraction does not yield the true vertical displacement; raw elevation changes are additionally influenced by local horizontal displacement magnitude and azimuth, slope aspect and angle, and surface roughness (e.g. Oskin et al., 2012). However, restricting the analysis to flat, smooth parts of the landscape limits these effects, such that the simple elevation change closely resembles the actual vertical displacement. Therefore we eliminated areas with slopes of >5° from both DTMs and differenced only those overlapping low-slope regions that exceed a certain cut-off in surface area. This reduced localized scatter in elevation changes to typically ∼1 m for small areas of >10 m^2, and ∼0.5 m for larger areas of >2000 m^2 (Fig. 4). In order to limit the effects of erosional and depositional processes, we also removed riverbeds, beaches and landslides from the analysis.

To verify that the remaining elevation change values are unbiased by horizontal motions, we independently computed three-dimensional (3-D) surface displacements at a few discrete locations by applying the Iterative Closest Point (ICP) algorithm to windowed subsets of the 2012 and 2016 point clouds (Nissen et al., 2012) (further details on the ICP methods are in Supplementary Material A, Text A3). East–west and north–south ICP components account for broad-scale features of the horizontal deformation field including lateral slip across the main surface ruptures, and verti-

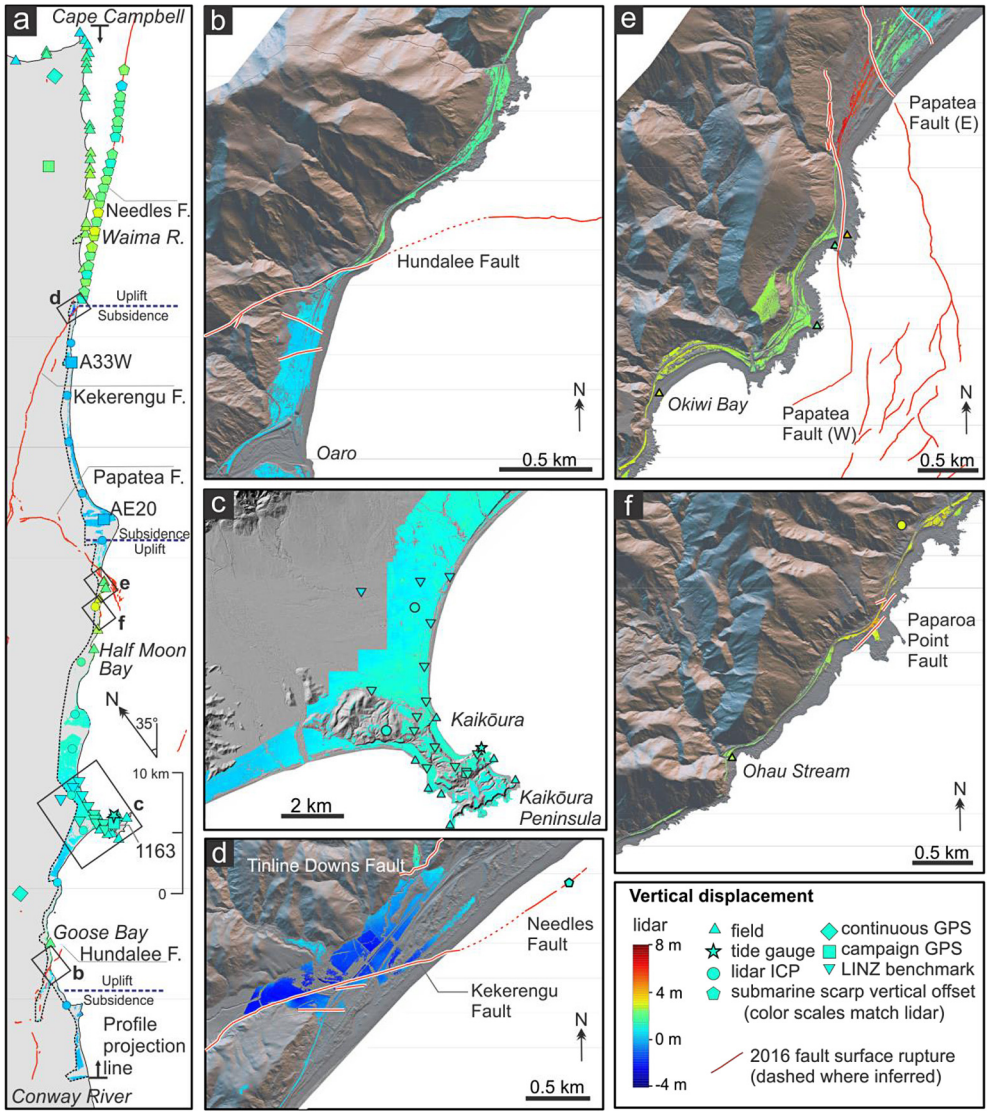

Fig. 3. Maps of coastal vertical displacement occurring in the 2016 Kaikōura earthquake. (a) Coastline impacted by Kaikōura earthquake, dashed black line shows the extent of overlapping pre- and post-earthquake lidar coverage, within which the color shaded areas represent the 0–5 degree slopes over which we measured 2016–2012 vertical displacement. The dark blue dashed lines delineate the hinge points between uplift and subsidence. (b)–(f) Detailed maps of areas of interest, particularly around fault surface ruptures. (For interpretation of the references to color in this figure legend, the reader is referred to the web version of this article.)

cal ICP components are in close agreement with nearby elevation change and field measurements (Fig. 4). This confirms that filtering of the lidar elevation changes for low slope angles ($<5°$) is effectual in eliminating potential biasing from horizontal deformation.

3.3. Offshore data and elastic dislocation modeling

Rupture of offshore faults including the Hundalee, Papatea, Needles and newly identified Point Kean fault (Fig. 1b) was mapped on two post-earthquake marine voyages using Kongsberg EM2040 and EM302 multibeam systems (the detailed methods of offshore data collection are in Supplementary Material A, Text A5). All these faults show clear surface traces on the seafloor and can be pinpointed as being co-seismic with the 2016 earthquake from pre- and post-earthquake surveys or the presence of scarps in the shallow water mobile sediment zone. In the case of the Point Kean fault which occurs on the outer shelf in ~50 m water depth, no knowledge of the Point Kean fault existed before the earthquake and therefore the co-seismic movement is uncertain. The offshore Hope fault was also re-surveyed in several locations using a TOPAS subbottom profiler but no change was found compared to the pre-earthquake bathymetry. These data indicate that no offshore rupture occurred on the Hope fault. Vertical offsets on the 2016 rupture scarp of the Needles fault were measured at approximately 1 km intervals in ArcGIS using fault normal bathymetric profiles, the offsets are assumed to equal the coseismic vertical slip (Supplementary Material A, Table A5).

The slip model for the earthquake was developed using the methods described in Hamling et al. (2017). Their initial fault model incorporates InSAR displacements in the satellite line-of-sight, campaign and continuous scattered GPS offsets and a limited number of field measurements of coastal uplift. Our refined fault geometry is based on their model but incorporates the new lidar measurements of coastal deformation and offshore fault vertical slip data.

3.4. Comparison between coastal deformation measurements

The Kaikoura earthquake coastal deformation dataset is primarily derived from estimates of uplift produced by two techniques, lidar differencing and field measurements. It is important to assess the agreement between the two techniques because they

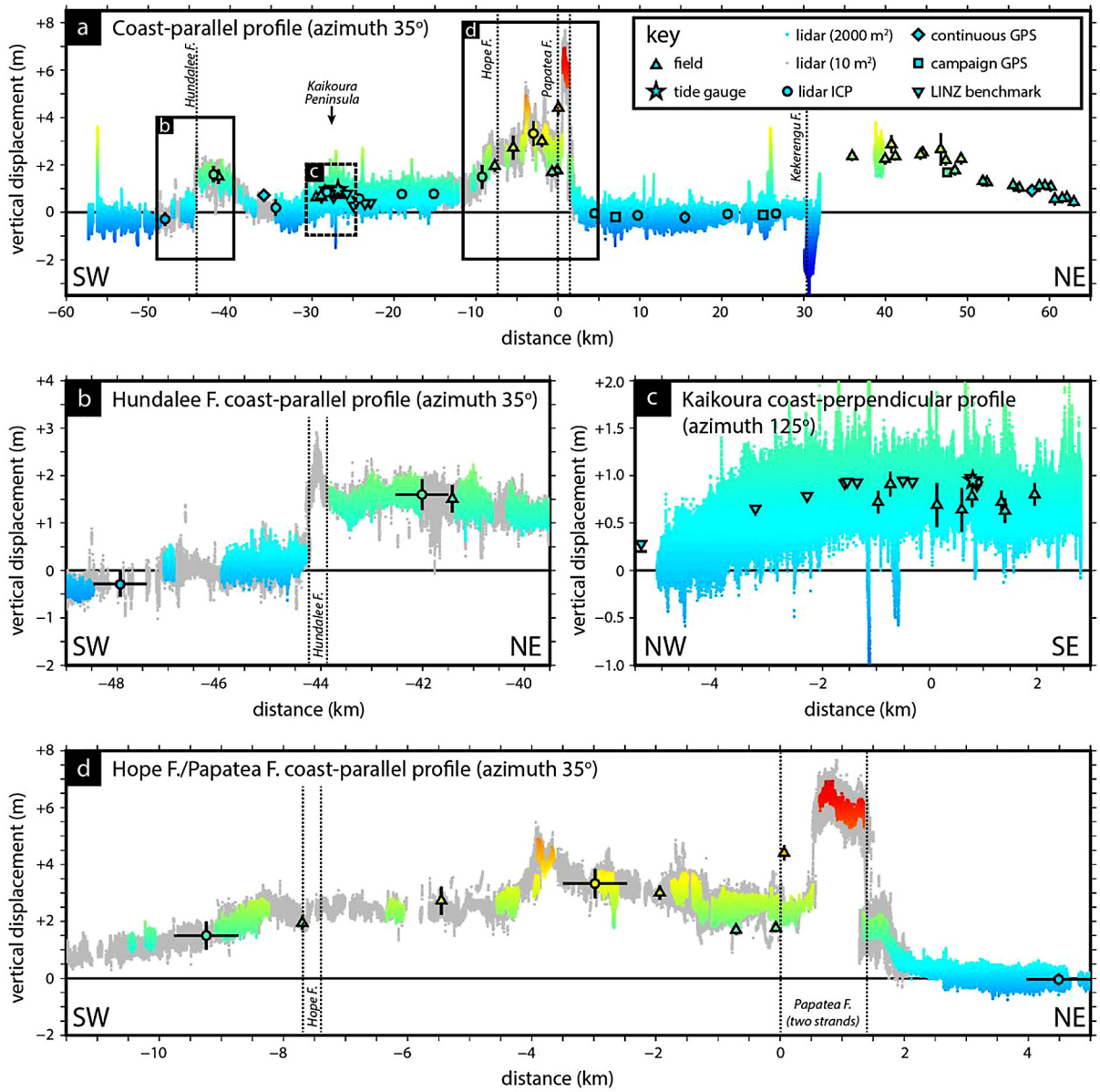

Fig. 4. (a) Field, lidar, and geodetic measurements of coseismic vertical deformation projected onto a straight line of azimuth 35° that roughly parallels the Kaikōura coastline, centered ($x = 0$) at the Papatea fault (the endpoints of the projection plane are shown on Fig. 3a). Vertical bars indicate 95% confidence bounds on the field, ICP, and GPS measurements (the latter are barely visible at this scale); vertical dashed lines indicate locations of major faults at the coastline. The color scale is the same as Fig. 3. Colored lidar points represent differential vertical movement calculated from overlapping surface areas >2000 m^2; the grey points represent surface areas >10 m^2. (b) Detail across the Hundalee fault. The horizontal bars around the ICP data points indicate the measurement aperture of ∼1 km for this method (see Supplementary Material Text A3). (c) Coastline-perpendicular uplift profile showing tilting across the Kaikōura Peninsula. Here, the profile azimuth is 125° and the projection center ($x = 0$) is at Kaikōura township. (d) Detailed coastline-parallel uplift measurements from across the Hope and Papatea faults.

cover different areas of coastal deformation along the rupture extent and systematic bias between the approaches could compromise interpretations. We have statistically assessed the agreement between the main sources of coastal uplift data and find almost no bias between the field measurements and lidar differencing results at fourteen coincident sites, this indicates sufficient agreement to treat them as equivalent for the purposes of interpretation (Supplementary Material A, Text A6, Fig. A6). Only three campaign GPS sites lie within the area of lidar double coverage, but here again the agreement is within the 2σ uncertainties (Supplementary Material A, Fig. A7). The campaign GPS sites were measured within 1 week of the Kaikōura earthquake, and prior to the earthquake they showed no significant vertical movement (<−2 mm/yr). Therefore, the campaign GPS and lidar should be measuring equivalent amounts of coseismic vertical movement. The agreement between campaign GPS and lidar, combined with the observation that field and lidar measurements are equivalent, demonstrates the robustness of the coastal deformation dataset along the entire 110 km of coastline resolved in this study.

The correspondence between the field, lidar and GPS uplift measurements with satellite radar-based estimates is more variable (Fig. 5). In addition to their elastic dislocation modeling, Hamling et al. (2017) combine smooth line-of-sight displacements (from SAR interferometry) with noisier horizontal offsets (from SAR amplitude pixel correlation) to map the regional deformation field in three dimensions. Resulting vertical displacements reproduce the large-scale features of the other coastal uplift datasets, including broad swells of uplift centered north of the Hundalee fault, at the Papatea fault, and north of the Kekerengu fault (Fig. 5a). However,

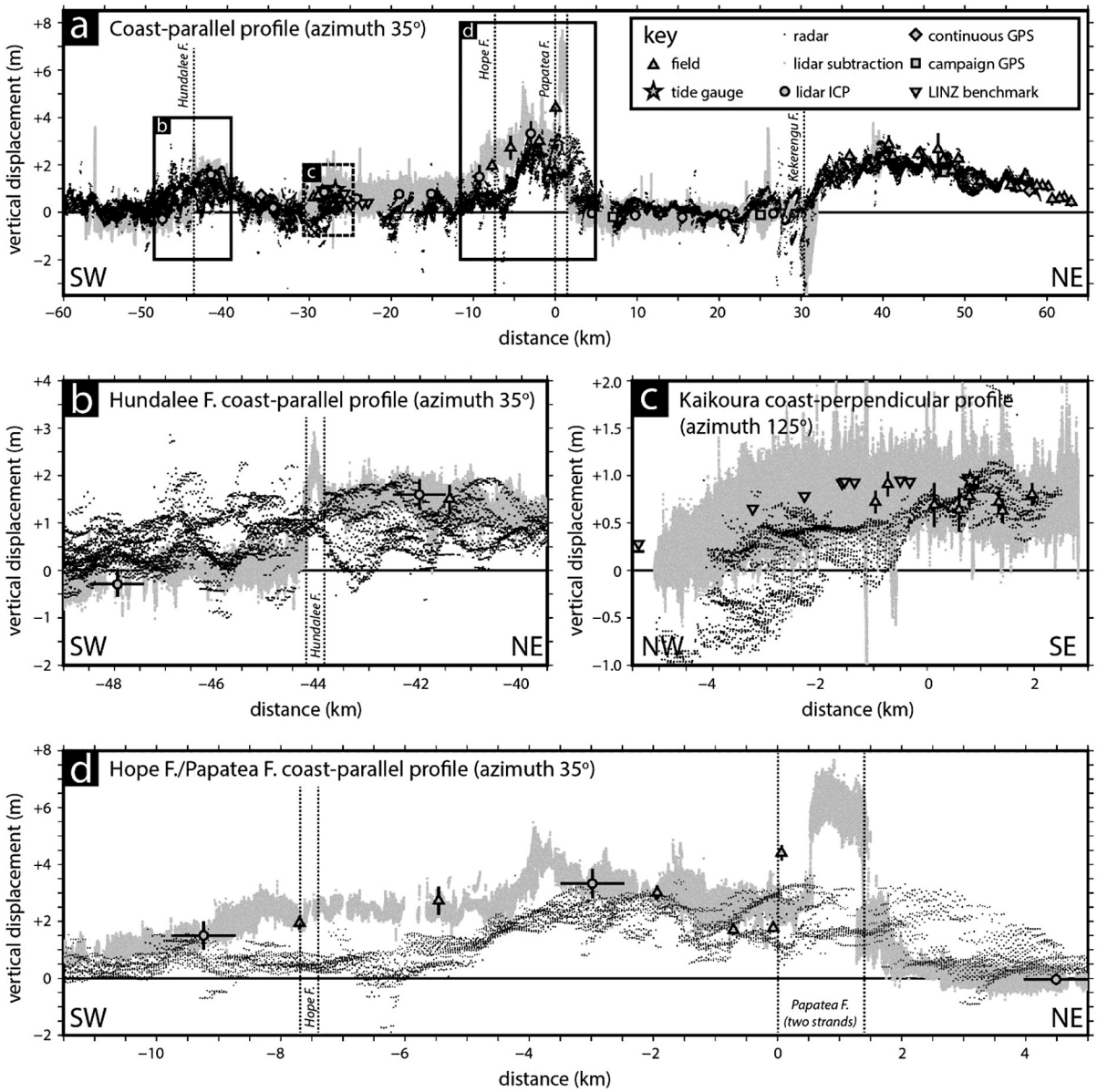

Fig. 5. (a) Comparison between radar-derived (InSAR plus SAR pixel offset) estimates of coastal vertical deformation (small black dots) with the field, lidar, and geodetic measurements shown in Fig. 4a (here shaded in grey). As with Fig. 4a, all data are projected onto a straight line of azimuth 35° that parallels the Kaikōura District coastline (Fig. 3a). The radar-derived uplift points are from a ∼3 km-wide swath along the coastline. (b) Detail from across the Hundalee fault. (c) Coastline- perpendicular profile across the Kaikōura Peninsula (azimuth 125°, projection center at Kaikōura township, as in Fig. 4c). (d) Detail from across the Hope and Papatea faults.

fine details such as slip across discrete faults – readily apparent in the lidar elevation changes – are obscured in the noisier radar uplift estimates (Fig. 5b, d). This indicates that although the radar measurements span a far broader region (>100 km) than the narrow coastal lidar swath, and nominally capture deformation in 3-D, they cannot resolve uplift patterns at the same fine spatial scale or with the same precision as the lidar.

4. Coastal deformation: south-west to north-east

Maps of coastal vertical displacement (Fig. 3) and projection of coastal deformation measurements onto a plane running SW–NE along the coastline (Fig. 4a) reveal a high level of variability over a range of length scales. Here we describe the coastal deformation from south-west to north-east, in the direction of rupture propagation, and relate uplift measurements to fault distribution.

4.1. Hundalee fault

The Hundalee fault marks the south-western limit of significant coastal uplift; south-west of the fault only minor (<0.5 m) coseismic subsidence and uplift occurred (Figs. 3b, 4b). There is 1.2 m of vertical offset at the main trace of the Hundalee fault; two minor fault traces with <0.4 m of vertical displacement occur south of the Hundalee fault. Two peaks in coastal uplift occur north–east of the Hundalee fault: a peak of 2.2 m at 0.1 km NE, and 1.6 m at 1.8 km NE; this short-wavelength variability attests to distributed fault zone deformation on- and offshore (Fig. 4b). North–east of Goose Bay uplift gradually decreases but notably no distinct vertical offset is seen across the coastal projection of the N–S striking Whites Lineament, a fault that has been identified by InSAR and estimated to have slip of 1–2 m at depth (Hamling et al., 2017), and seen to have intermittent surface rupture >3 km inland (Litchfield et al., 2017) (Fig. 1b).

4.2. Kaikōura Peninsula

Uplift of 0.8–1 m is recorded from 4 km south to 16 km north of the Kaikōura Peninsula (Figs. 3a, 4a). The relatively wide range (∼1 m) in differential lidar uplift measurements across this area reflects the wider inland extent of joint lidar coverage combined with a small degree of coseismic landward tilting (Fig. 4c) which produces scatter when the points are projected to a plane (Fig. 4a). There is a relatively uniform uplift profile of 0.8–0.95 m across the Kaikōura Peninsula (Fig. 4c), although slightly lower field and lidar measurements on the southern coast show a degree of tilt, down to the southwest, across the Peninsula. The Kaikōura Peninsula fault has been inferred offshore of the peninsula by Barrell (2015) based on the distribution of Holocene marine terraces, and the Point Kean fault (Fig. 1b) has been identified northeast of the peninsula based on seafloor scarps and a region of folded strata (eroded strike ridges). The location of the Point Kean fault in respect to the broad, low amplitude coastal uplift seen along the ∼25 km stretch of coastline surrounding Kaikōura Peninsula, and the tentatively identified fresh rupture scarp, suggests it could be a candidate for explaining the onshore deformation, this is further explored in the discussion.

4.3. Hope fault to Papatea fault

The 13 km stretch of steep and rocky coastline from 3 km south–west of the Hope fault to the Papatea fault displays large uplift values (mostly >2 m) and high variability related to three surface fault ruptures, along with possible contributions from nearshore faults that may run sub-parallel with the coast (Figs. 3e, 3f, 4d).

There is a distinct 1 m increase in coastal uplift from 2 km to 0.5 km south–west of the Hope fault and then a decrease toward the surface rupture trace (Fig. 4d). Field measurements of the surface trace of the Hope fault, at Half Moon Bay, showed ∼0.4 m vertical offset (up to the NW) and negligible dextral slip, although no other surface rupture was seen along the onshore Hope fault and resurveys of known traces of the offshore Hope fault show no new rupture. Minor offset (<0.5 m) in the lidar differencing measurements across the surface rupture is consistent with the field observations. Slip modeling by Hamling et al. (2017) suggested localized slip (predominantly strike-slip) of almost 3–4 m in the upper 3 km of the seaward part of the Hope fault but noted that limited data and local inelastic effects make this poorly constrained. Thus the role of the Hope fault in terms of coseismic slip in the Kaikōura earthquake is poorly constrained, but of particular interest, because if it did not slip in the earthquake the northward propagating surface rupture would have largely jumped over the highest slip rate fault in the Marlborough fault system. Coastal uplift south of the Hope fault suggests slip on a blind fault in the area between the Hope fault and the Mangamaunu faults (Barrell, 2015) (Supplementary Material A, Fig. A8), and is therefore consistent with the general location of modeled slip (Hamling et al., 2017), but not necessarily with it being on the main trace of the Hope fault.

North–east of the Hope fault the coastal uplift is consistent at 2–2.5 m for ∼3 km along the coast before increasing sharply within 1 km of Paparoa Point (Fig. 3f). Across Paparoa Point three minor fault scarps of the Paparoa Point fault strike subparallel to the coast and have vertical offsets of 0.3–1 m, each upthrown to the NW. The relationship between the Paparoa Point and Papatea faults is not clear but the complex rupture pattern of the offshore Papatea fault includes NNE-striking splays consistent with the strike of the Paparoa Point fault traces (Fig. 3e).

Between the Paparoa Point and Papatea faults, coastal uplift generally decreases (Fig. 4d). Minor variations on the order of <1 m of uplift suggest either slip on nearshore faults or varying slip distribution across the offshore, southwest-dipping Papatea fault. The Papatea fault splays into two strands at the coastline and the popup block between the strands records the maximum coastal uplift for the Kaikōura earthquake of 6.6 ± 0.5 m (Figs. 3e, 4d). Vertical offset across the western fault strand is 3.5 m up to the east, and across the eastern strand of the Papatea fault there is 4 m of vertical offset, down to the east. The relatively wide range (1–1.5 m) of lidar and field measurements across the Papatea fault is due to tilt of the uplifted fault block toward the profile projection line (Fig. 4d). Half a kilometer north–east of the western strand of the Papatea fault, another minor fault trace shows a ∼0.5 m vertical step (down to NE); further north–east still, coastal uplift steadily decreases.

4.4. Kekerengu–Needles fault

This earthquake has shown that the Kekerengu and Needles faults are likely to be the same continuous fault. Offshore, the fresh rupture scarp of the Needles fault has been mapped to within 600 m of where the Kekerengu fault rupture meets the coast (Fig. 3a). Localized subsidence of up to 2.5 m over a width of 200–400 m occurs on both sides of the Kekerengu fault (Figs. 3d, 4a). This may be due to interplay between oblique normal behavior of the Kekerengu fault at this easterly-striking bend on the fault, contributions from minor faults south of the main trace (Fig. 3d), downthrow of the footwall of the Tinline Downs fault, and soft sediment compaction in the stream valley.

The amount of localized subsidence measured around the Kekerengu fault by lidar differencing is surprisingly large, but it is of an order of magnitude greater than the vertical uncertainty typical of lidar. Field observations also provide evidence of subsidence: immediately after the earthquake, a significant area of ponded water appeared on both sides of the Kekerengu fault where there had formerly been only a shallow stream (Supplementary Material A, Fig. A9). Ponded water still persists at 7 months after the earthquake indicating the stream base level has permanently shifted. Satellite radar and optical imagery-based models of ground deformation (Hamling et al., 2017; Hollingsworth et al., 2017), have not observed the localized subsidence despite its significant magnitude; this demonstrates the advantage of lidar differencing in terms of capturing fine-scale fault zone deformation and secondary effects of fault rupture.

North of the Kekerengu fault, and inboard of the Needles fault, there is a change to coastal uplift on the order of 2–3 m. From a peak of 2.9 m near the Waima River, there is a north–eastward decrease in coastal uplift to 0.4 m at Cape Campbell (with a 0.5 m step across the Lighthouse fault, 2.5 km south of Cape Campbell). This north–eastward decrease largely mimics the scarp heights on the fresh rupture trace of the submarine Needles fault and is a function of both diminishing slip on the Needles fault (Supplementary Material A, Table A5) and increasing distance between the coastline and the Needles fault (Fig. 3a).

5. Discussion

The coastal deformation record of the 2016 Kaikōura earthquake is primarily characterized by high spatial variability; no record of comparable complexity has been documented in recent times. The majority of recent coseismic coastal deformation observations are related to subduction earthquakes in which the deformation is characterized by arc-parallel zones of uplift and subsidence with long wavelength variability (>10's kms) related to heterogeneous slip on a single principal fault, and, less commonly, short wavelength variability due to splay fault rupture (e.g. Briggs et al., 2006; Melnick et al., 2012b; Plafker, 1969;

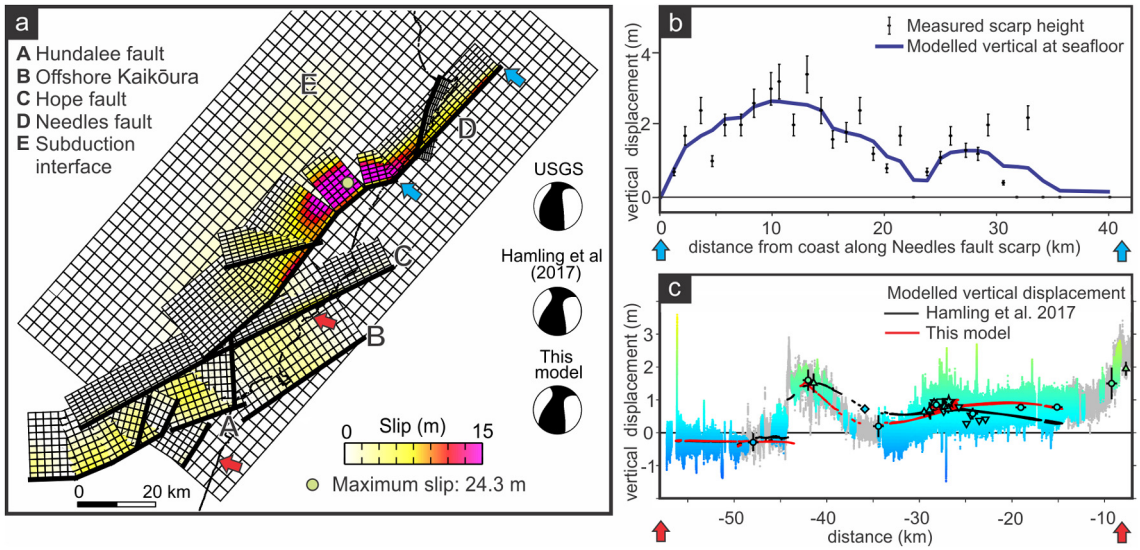

Fig. 6. (a) Best fitting slip model for the Kaikōura earthquake based on inversion of geodetic and coastal deformation data (see section 3.3 for details). Moment tensors show the USGS CMT solution and the equivalent for the Hamling et al. (2017) model and the model produced for this study. Heavy black lines denote the top edge of the fault surface. Note the Papatea fault is not included in this model, see Hamling et al. (2017) for discussion. (b) Fit between the modeled vertical displacement and vertical displacement along the 2016 rupture scarp of the Needles fault. (c) Fit between the modeled vertical displacement and compiled vertical displacement measurements (see key in Fig. 4) from the Conway River to north of Kaikōura Peninsula. This plot demonstrates improved fit using the refined dislocation model of this study compared to the model of Hamling et al. (2017) which omitted a crustal fault offshore of Kaikōura Peninsula.

Plafker and Savage, 1970; Subarya et al., 2006). Coastal uplift observations following crustal earthquakes has usually been associated with nearshore reverse faulting, and the observations have also typically been consistent with single fault ruptures (e.g. Awata et al., 2008; Meghraoui et al., 2004). Variable coastal uplift in the 2007 M_W7.0 Haiti earthquake reflected the complexity of multi-fault rupture, albeit on a lesser scale than Kaikōura with maximum uplift of 0.65 m (Hayes et al., 2010). The complex coastal deformation record presented in this study has implications for both the fault source model of the Kaikōura earthquake and paleoseismic reconstructions of past earthquakes.

5.1. Refined slip model and implications for involvement of the subduction interface

The high-resolution record of coastal deformation presented in this study enables a more complete picture of offshore fault rupture, slip distributions, and tsunamigenesis associated with the earthquake. The slip model for the Kaikōura earthquake developed by Hamling et al. (2017) exploited some field measurements of coastal uplift, but the greatly increased resolution and continuity of the coastal deformation record presented here warrants reassessment of some offshore components of the slip model. Here we focus on two areas, the Needles fault and offshore Kaikōura Peninsula, where new data contribute to refining the earthquake slip model (Fig. 6a).

Along the Needles fault, the precise post-earthquake mapping of the 2016 rupture scarp inshore of the pre-earthquake fault trace result in the modeled fault plane shifting further inshore, and the amount of reverse slip is reduced by ∼1–2 m. This is a rare example (cf. Escartín et al., 2016; Fujiwara et al., 2011) of where measurement of coseismic vertical slip at the scarp of a submarine rupture can be used to constrain a slip model of an offshore fault (Fig. 6b).

The low-amplitude (∼1 m), broad wavelength uplift of the coast surrounding the Kaikōura Peninsula was not previously well-resolved by radar (Fig. 5) and so the geometry of uplift defined by lidar allows development of a more refined fault model for offshore Kaikōura Peninsula. Previously Hamling et al. (2017) modeled uplift of Kaikōura Peninsula along a linear extension of the Hundalee fault that stopped ∼3 km NE of the Peninsula. However, marine surveying carried out following the Kaikoura Earthquake indicates that surface rupture of the Hundalee fault probably terminates near the rim of the Kaikōura Canyon (Fig. 1). A structure identified on the outer shelf (the Point Kean fault) has been tested to see if it could be responsible for the uplift extending 20 km north of Kaikōura Peninsula. A NE-striking reverse fault, dipping 35° with ∼3 m of predominantly reverse slip extending to depths of 20 km is added to the slip model (Fig. 6a). This fault plane continues for ∼20 km north–east of Kaikōura Peninsula and the rupture would have displaced a broad area of the shelf. Our preliminary tsunami model using the revised offshore fault geometries indicate the reverse fault provides a significantly better fit for the 24 min, ∼2 m drawdown of sea-level observed on the Kaikōura tide gauge (Supplementary Material A, Fig. A10) compared to the model provided in Hamling et al. (2017) which could not replicate the initial prolonged drawdown at Kaikōura.

It currently remains debated as to whether there was slip on the southern end of the Hikurangi subduction interface during the 2016 Kaikōura earthquake (Furlong and Herman, 2017); generally, models using teleseismic data converge on a significant component of slip on the subduction interface, while geodetic observations point to dominantly crustal faulting with limited subduction interface involvement. Hollingsworth et al. (2017) use optical satellite imagery and inversion of teleseismic waveforms to develop a two-fault model of the Kekerengu fault and a deeper shallow-dipping fault (possibly the subduction interface) underlying the Kaikōura coastline. Similarly, Duputel and Rivera (2017) developed a four-point source inversion using teleseismic waves and identified a shallow dipping thrust fault and suggested this could be the subduction interface, or a forearc thrust fault. Bai et al. (2017) use iterative forward modeling of tide gauge records and teleseismic waves to model two regions of seafloor deformation in the Kaikōura earthquake. One region corresponds to the Needles Fault and the other, north of Kaikōura Peninsula, corresponds to a shallow dipping fault which they infer relates to an M_W7.6 rupture of the subduction interface. In contrast, using an inversion of geodetic data (InSAR and GPS) and coastal uplift field measurements, Hamling et al. (2017) modeled slip of ∼4 m on the plate interface inland of Kaikōura, although they note the contribution of the in-

terface source to the seismic moment is minor (15% if limited to an M_W7.9) compared with the crustal faults. Furthermore, a model with only crustal fault sources provides a similar level of fit to the geodetic data.

The coastal deformation record presented in this study is consistent with an offshore reverse fault northeast of the Kaikōura Peninsula, and although the geometry at depth is poorly constrained, the pattern of coastal uplift is more consistent with a shallow source. Maximum uplift of the Kaikoura Peninsula reaches ∼1 m but drops to close to zero over a 4 km length scale (Fig. 4c). At this location, the depth to the interface is ∼19 km – too deep to explain such short wavelength variations. In the refined dislocation model presented here (modified from Hamling et al., 2017; Fig. 6a), we still require slip on the deeper portion of the interface source to explain the observed subsidence inland. However, the addition of the new crustal fault source offshore of Kaikōura Peninsula, which is predicted to have slip of ∼3 m, reduces the amount of slip required on the interface to 1–2 m, while still fitting the observed uplift pattern (Fig. 6c) and global moment tensor (Fig. 6a). The dislocation model of Hamling et al. (2017) that had up to 4 m of slip on the plate interface, without an offshore fault, does not fit the distinct decrease in coastal uplift south–west of Kaikōura Peninsula (Fig. 6c).

Currently, the strongest evidence of plate interface slip in the Kaikōura earthquake comes from Bai et al. (2017) and although their fault model fits the teleseismic and tide gauge data well, it does not entirely reconcile with the coastal deformation record compiled in this study. Compatibility with the coastal deformation record is achieved inshore of the Kekerengu–Needles fault where up to 3 m of uplift is modeled and at Kaikōura Peninsula where 1 m of uplift is modeled. However, southwest of Kaikōura Peninsula a low-amplitude subsidence signal (largely driven by subsidence at the downdip end of the subduction interface rupture patch) contrasts to the coastal deformation record which shows uplift along most of the coastline from Kaikōura Peninsula to the Hundalee fault (Figs. 3a, 4a). Bai et al. (2017) model a broad area of uplift northeast of Kaikōura Peninsula, which is of similar amplitude to the coastal deformation record for approximately 15 km northeast of the Peninsula. However, the modeled maximum uplift of 0.9 m at 20 km northeast of Kaikōura Peninsula occurs where we measure 2–2.5 m of uplift. Furthermore, their model extends uplift to 40 km northeast of Kaikōura Peninsula, contrasting with measured coastal subsidence northeast of the Papatea fault, at 30 km northeast of Kaikōura Peninsula. Some of these differences are explained by slip on the Papatea fault, which Bai et al. (2017) acknowledge is not included as fault source (nor is it included in the dislocation model we present in Fig. 6a). To summarize, the 3-fault model of Bai et al. (2017), which includes up to 6 m of subduction interface slip, fits the tide gauge and teleseismic data well but areas of mismatch to the coastal deformation record indicate greater complexity in offshore faulting than they account for; we suggest that until these datasets are reconciled the amount and location of slip on the subduction interface remains uncertain.

5.2. Recognition of multi-fault ruptures in the coastal paleoseismic record

The complexity of coastal deformation in the Kaikōura earthquake raises potential pitfalls in mapping the extent of past coseismic uplift by along-coast continuity. Raised Holocene coastal geomorphology (e.g. marine terraces, beach ridges, tidal notches) is often used to record past earthquakes (e.g. Merritts, 1996; Rockwell et al., 2016). Along-coast continuity of uplifted coastal geomorphology and/or age correlation are typically used to assign synchronicity of uplift to features and thereby attribute them to a single earthquake (e.g. Hsieh and Rau, 2009; Shaw et al., 2008). The length and amount of coastal uplift can be used to infer paleoearthquake magnitudes (Berryman et al., 2011; Ramos and Tsutsumi, 2010).

If the Kaikōura earthquake were to be reconstructed from geological evidence, we would likely infer 3–4 separate earthquakes based on the highpoints of coastal uplift. Based on comparison with global historical observations of coastal uplift in comparatively simple fault ruptures, one marine terrace would likely be correlated with one planar offshore fault rupture, and therefore the paleoearthquake magnitude would also be underestimated. Age correlation would not greatly help in resolving synchronous uplift on spatially separated terraces because the resolution of conventional dating methods (e.g. radiocarbon) could not distinguish between two spatially distant marine terraces uplifted in the same earthquake, as opposed to two or more earthquakes closely spaced in time. The record of highly variable coastal uplift in the Kaikōura earthquake should motivate re-thinking of coastal paleoseismic records to give greater consideration to multi-fault ruptures, particularly at complex plate boundaries. Such re-assessment of the ability of various paleoseismic methods to determine past occurrence of complex multi-fault earthquakes is a key lesson from the 2016 M_W7.8 Kaikōura earthquake.

6. Conclusions

The 2016 Kaikōura earthquake is one of the most complex earthquakes ever recorded (Hamling et al., 2017), and the high variability in vertical deformation along 110 km of coastline reflects the rupture complexity. Sharp changes in coastal deformation are recorded at the surface ruptures of the Hundalee, Papatea and Kekerengu faults, while lower amplitude variability in coastal uplift reflects distributed deformation near the major fault surface ruptures, minor fault surface ruptures and slip on nearshore faults subparallel to the coastline. A high resolution dataset of coastal deformation contributes to better constraint on offshore fault ruptures. In this case, broad uplift of the Kaikoura Peninsula area, precisely defined by lidar differencing but not well resolved by satellite geodesy, reveals the involvement of an offshore reverse fault in the forearc crust. The highly variable nature of the coastal deformation associated with the Kaikōura earthquake should lead to the re-examination of how uplifted coastal geomorphology is used in paleoseismic studies to interpret past earthquakes and inform seismic hazard. Multi-fault rupture scenarios may be underrepresented in paleoseismology due to the prevalence of relatively simple fault sources in historic examples of coastal deformation.

Acknowledgements

Funding for the post-earthquake coastal uplift field survey and subsequent analysis was provided by GeoNet, with the support of its sponsors New Zealand Earthquake Commission (EQC), GNS Science, and Land Information New Zealand, and Ministry of Business, Innovation and Employment (MBIE) response funding, provided through the Natural Hazards Research Platform (grant 2017-GNS-01-NHRP), and GNS Science MBIE strategic science investment funding (GNS-SSIF-TSZ). Land Information New Zealand, New Zealand Transport Authority, Environment Canterbury, Marlborough District Council, Aerial Surveys Ltd and AAM NZ Ltd are thanked for providing high quality lidar data. The 2012 lidar data (http://dx.doi.org/10.5069/G98C9T67) and derived products are hosted and disseminated by the OpenTopography Facility (http://www.opentopography.org/) with support from the US National Science Foundation under NSF Awards 1226353 and 1225810. Biljana Lukovic and Dave Heron are thanked for readily providing GIS

support and logistical support in the field was provided by Zoe Juniper. Funding for the offshore fault mapping work with *RV Ikatere* was provided by MBIE through the Natural Hazards Research Platform (grant C05X0907). NIWA survey staff Susi Woelz, Tim Kane and Will Quinn collected and processed the marine data and we thank the *RV Ikatere* crew for completing the marine field work in challenging conditions. Whalewatch Kaikōura are thanked for their support during this and previous offshore fieldwork campaigns. The RV Tangaroa survey was funded by MBIE through the Endeavour Fund (grants C05X1605 and COPR1702) and the Tangaroa Reference Group. We thank Laura Wallace and an anonymous reviewer for their comments on the manuscript.

Appendix A. Supplementary material

Supplementary material related to this article can be found online at http://dx.doi.org/10.1016/j.epsl.2017.06.048.

References

Awata, Y., Toda, S., Kaneda, H., Azuma, T., Horikawa, H., Shishikura, M., Echigo, T., 2008. Coastal deformation associated with the 2007 Noto Hanto earthquake, central Japan, estimated from uplifted and subsided intertidal organisms. Earth Planets Space 60, 1059–1062.

Bai, Y., Lay, T., Cheung, K.F., Ye, L., 2017. Two regions of seafloor deformation generated the tsunami for the 13 November 2016, Kaikoura, New Zealand earthquake. Geophys. Res. Lett. http://dx.doi.org/10.1002/2017GL073717.

Barrell, D.J.A., 2015. General Distribution and Characteristics of Active Faults and Folds in the Kaikoura District, North Canterbury. GNS Science Consultancy Report 2014/210, Environment Canterbury Report No. R15/23. 59 pp.

Berryman, K., Ota, Y., Miyauchi, T., Hull, A., Clark, K., Ishibashi, K., Iso, N., Litchfield, N., 2011. Holocene paleoseismic history of upper-plate faults in the southern Hikurangi subduction margin, New Zealand, deduced from Marine Terrace Records. Bull. Seismol. Soc. Am. 101, 2064–2087.

Bodin, P., Klinger, T., 1986. Coastal uplift and mortality of intertidal organisms caused by the September 1985 Mexico earthquakes. Science 233, 1071–1073.

Briggs, R.W., Sieh, K., Meltzner, A., Natawidjaja, D., Galetzka, J., Suwargadi, B., Hsu, Y., Simons, M., Hananto, N., Suprihanto, I., Prayudi, D., Avouac, J.-P., Prawirodirdjo, L., Bock, Y., 2006. Deformation and slip along the Sunda Megathrust in the great 2005 Nias–Simeulue earthquake. Science 311, 1897.

Duputel, Z., Rivera, L., 2017. Long-period analysis of the 2016 Kaikōura earthquake. Phys. Earth Planet. Inter. 265, 62–66.

Escartín, J., Leclerc, F., Olive, J.-A., Mevel, C., Cannat, M., Petersen, S., Augustin, N., Feuillet, N., Deplus, C., Bezos, A., Bonnemains, D., Chavagnac, V., Choi, Y., Godard, M., Haaga, K.A., Hamelin, C., Ildefonse, B., Jamieson, J.W., John, B.E., Leleu, T., MacLeod, C.J., Massot-Campos, M., Nomikou, P., Paquet, M., Rommevaux-Jestin, C., Rothenbeck, M., Steinführer, A., Tominaga, M., Triebe, L., Campos, R., Gracias, N., Garcia, R., Andreani, M., Vilaseca, G., 2016. First direct observation of coseismic slip and seafloor rupture along a submarine normal fault and implications for fault slip history. Earth Planet. Sci. Lett. 450, 96–107.

FitzRoy, R., 1839. Proceedings of the Second Expedition, 1831–1836, Under the Command of Captain Robert FitzRoy. Volume II of the narrative of the surveying voyages of His Majesty's ships Adventure and Beagle between Years 1826 and 1836, describing their examination of the southern shores of South America, and the Beagle's circumnavigation of the globe. London, UK.

Fujiwara, T., Kodaira, S., No, T., Kaiho, Y., Takahashi, N., Kaneda, Y., 2011. The 2011 Tohoku–Oki earthquake: displacement reaching the trench axis. Science 334, 1240.

Furlong, K., Herman, M., 2017. Reconciling the deformational dichotomy of the 2016 Mw 7.8 Kaikoura NZ earthquake. Geophys. Res. Lett. http://dx.doi.org/10.1002/2017GL074365.

Hamling, I., Hreinsdóttir, S., Clark, K., Elliott, J., Liang, C., Fielding, E.J., Litchfield, N., Villamor, P., Wallace, L., Wright, T.J., D'Anastasio, E., Bannister, S., Burbridge, D., Denys, P., Gentle, P., Howarth, J., Mueller, C., Palmer, N., Pearson, C., Power, W., Barnes, P., Barrell, D., Van Dissen, R., Langridge, R., Little, T., Nicol, A., Pettinga, J., Rowland, J., Stirling, M., 2017. Complex multi-fault rupture during the 2016 Mw 7.8 Kaikōura earthquake, New Zealand. Science. http://dx.doi.org/10.1126/science.aam7194.

Hamling, I.J., D'Anastasio, E., Wallace, L.M., Ellis, S., Motagh, M., Samsonov, S., Palmer, N., Hreinsdóttir, S., 2014. Crustal deformation and stress transfer during a propagating earthquake sequence: the 2013 Cook Strait sequence, central New Zealand. J. Geophys. Res., Solid Earth 119, 6080–6092.

Hayes, G.P., Briggs, R.W., Sladen, A., Fielding, E.J., Prentice, C., Hudnut, K., Mann, P., Taylor, F.W., Crone, A.J., Gold, R., Ito, T., Simons, M., 2010. Complex rupture during the 12 January 2010 Haiti earthquake. Nat. Geosci. 3, 800–805.

Hollingsworth, J., Ye, L., Avouac, J.-P., 2017. Dynamically triggered slip on a splay fault in the Mw 7.8, 2016 Kaikoura (New Zealand) earthquake. Geophys. Res. Lett. 44. http://dx.doi.org/10.1002/2016GL072228.

Hsieh, M.-L., Rau, R.-J., 2009. Late Holocene coseismic uplift on the Hua-tung coast, eastern Taiwan: evidence from mass mortality of intertidal organisms. Tectonophysics 474, 595–609.

Jaramillo, E., Melnick, D., Baez, J.C., Montecino, H., Lagos, N.A., Acuña, E., Manzano, M., Camus, P.A., 2017. Calibrating coseismic coastal land-level changes during the 2014 Iquique (Mw = 8.2) earthquake (northern Chile) with leveling, GPS and intertidal biota. PLoS ONE 12, e0174348.

Kaiser, A.E., Balfour, N., Fry, B., Holden, C., Litchfield, N., Gerstenberger, M., D'Anastasio, E., Horspool, N., McVerry, G., Ristau, J., Gledhill, K., Bannister, S., Christopherson, A., Clark, K., Power, W., Rhoades, D., Hamling, I., Wallace, L., Mountjoy, J., Kaneko, Y., Benites, R.A., Van Houtte, C., Massey, C., Dellow, S., Hreinsdottir, S., 2017. The 2016 Kaikōura (New Zealand) earthquake: preliminary seismological report. Seismol. Res. Lett. 88 (3). http://dx.doi.org/10.1785/0220170018.

Konca, A.O., Hjorleifsdottir, V., Song, T.-R.A., Avouac, J.-P., Helmberger, D.V., Ji, C., Sieh, K., Briggs, R., Meltzner, A., 2007. Rupture kinematics of the 2005 Mw 8.6 Niasâ–Simeulue earthquake from the joint inversion of seismic and geodetic data. Bull. Seismol. Soc. Am. 97, S307–S322.

Langridge, R.M., Ries, W.F., Litchfield, N.J., Villamor, P., Van Dissen, R.J., Barrell, D.J.A., Rattenbury, M.S., Heron, D.W., Haubrock, S., Townsend, D.B., Lee, J.M., Berryman, K.R., Nicol, A., Cox, S.C., Stirling, M.W., 2016. The New Zealand active faults database. N.Z. J. Geol. Geophys. 59, 86–96.

Litchfield, N.J., Van Dissen, R.J., Sutherland, R., Barnes, P.M., Cox, S.C., Norris, R., Beavan, R.J., Langridge, R., Villamor, P., Berryman, K., Stirling, M., Nicol, A., Nodder, S., Lamarche, G., Barrell, D.J.A., Pettinger, J.R., Little, T.A., Pondard, N., Mountjoy, J.J., Clark, K., 2014. A model of active faulting in New Zealand. N.Z. J. Geol. Geophys. 57, 32–56.

Litchfield, N.J., Benson, A., Bischoff, A., Hatem, A., Barrier, A., Nicol, A., Wandres, A., Lukovic, B., Hall, B., Gasston, C., Asher, C., Grimshaw, C., Madugo, C., Fenton, C., Hale, D., Barrell, D.J.A., Heron, D.W., Strong, D.T., Townsend, D.B., Noble, D., Howarth, J.D., Pettinga, J., Kearse, J., Williams, J., Manousakis, J., Mountjoy, J., Rowland, J., Clark, K.J., Pedley, K., Sauer, K., Berryman, K.R., Hemphill-Haley, M., Stirling, M.W., Villeneuve, M., Cockroft, M., Khajavi, N., Barnes, P., Villamor, P., Carne, R., Langridge, R.M., Zinke, R., Van Dissen, R.J., McColl, S., Cox, S.C., Lawson, S., Little, T., Stahl, T., Cochran, U.A., Toy, V., Ries, W.F., Juniper, Z., 2017. 4th November 2016 M7.8 Kaikōura earthquake. Summary surface fault traces and preliminary displacement measurements. http://dx.doi.org/10.21420/G21422RC21427C.

Meghraoui, M., Maouche, S., Chemaa, B., Cakir, Z., Aoudia, A., Harbi, A., Alasset, P.J., Ayadi, A., Bouhadad, Y., Benhamouda, F., 2004. Coastal uplift and thrust faulting associated with the Mw = 6.8 Zemmouri (Algeria) earthquake of 21 May, 2003. Geophys. Res. Lett. 31, L19605. http://dx.doi.org/10.1029/2004GL020466.

Melnick, D., Cisternas, M., Moreno, M., Norambuena, R., 2012a. Estimating coseismic coastal uplift with an intertidal mussel: calibration for the 2010 Maule Chile earthquake (Mw = 8.8). Quat. Sci. Rev. 42, 29–42.

Melnick, D., Moreno, M., Motagh, M., Cisternas, M., Wesson, R.L., 2012b. Splay fault slip during the Mw 8.8 2010 Maule Chile earthquake. Geology 40, 251–254.

Meltzner, A.J., Sieh, K., Abrams, M., Agnew, C.D., Hudnut, K.W., Avouac, J.-P., Natawidjaja, D.H., 2006. Uplift and subsidence associated with the great Aceh–Andaman earthquake of 2004. J. Geophys. Res. 111. http://dx.doi.org/10.1029/2005Jb003891.

Merritts, D.J., 1996. The Mendecino triple junction: active faults, episodic coastal emergence, and rapid uplift. J. Geophys. Res. 101, 6051–6070.

Nissen, E., Krishnan, A.K., Arrowsmith, J.R., Saripalli, S., 2012. Three-dimensional surface displacements and rotations from differencing pre- and post-earthquake LiDAR point clouds. Geophys. Res. Lett. 39, L16301.

Oskin, M.E., Arrowsmith, J.R., Corona, A.H., Elliott, A.J., Fletcher, J.M., Fielding, E.J., Gold, P.O., Garcia, J.J.G., Hudnut, K.W., Liu-Zeng, J., Teran, O.J., 2012. Near-field deformation from the El Mayor–Cucapah earthquake revealed by differential LIDAR. Science 335, 702–705.

Ota, Y., Pillans, B., Berryman, K., Beu, A., Fujimori, T., Miyauchi, T., Berger, G., Beu, A., Climo, F., 1996. Pleistocene coastal terraces of Kaikōura Peninsula and the Marlborough Coast, South Island, New Zealand. N.Z. J. Geol. Geophys. 39, 51–73.

Plafker, G., 1969. Tectonics of the March 27, 1964, Alaska Earthquake. Geological Survey Professional Paper 543-1. 174 pp.

Plafker, G., Savage, J.C., 1970. Mechanism of the Chilean Earthquakes of May 21 and 22, 1960. Geol. Soc. Am. Bull. 81, 1001–1030.

Power, W., Clark, K., King, D.N., Borrero, J., Howarth, J., Lane, E.M., Goring, D., Goff, J., Chagué-Goff, C., Williams, J., Reid, C., Whittaker, C., Mueller, C., Williams, S., Hughes, M.W., Hoyle, J., Bind, J., Strong, D., Litchfield, N., Benson, A., 2017. Tsunami runup and tide-gauge observations from the 14 November 2016 M7.8 Kaikōura earthquake, New Zealand. Pure Appl. Geophys. 174, 2457. http://dx.doi.org/10.1007/s00024-017-1566-2.

Ramos, N.T., Tsutsumi, H., 2010. Evidence of large prehistoric offshore earthquakes deduced from uplifted Holocene marine terraces in Pangasinan Province, Luzon Island, Philippines. Tectonophysics 495, 145–158.

Rockwell, T.K., Clark, K., Gamble, L., Oskin, M.E., Haaker, E.C., Kennedy, G.L., 2016. Large transverse range earthquakes Cause Coastal Upheaval near Ventura, Southern California. Bull. Seismol. Soc. Am. 106, 2706–2720.

Shaw, B., Ambraseys, N.N., England, P.C., Floyd, M.A., Gorman, G.J., Higham, T.F.G., Jackson, J.A., Nocquet, J.M., Pain, C.C., Piggott, M.D., 2008. Eastern Mediterranean tectonics and tsunami hazard inferred from the AD 365 earthquake. Nat. Geosci. 1, 268–276.

Subarya, C., Chlieh, M., Prawirodirdjo, L., Avouac, J.-P., Bock, Y., Sieh, K., Meltzner, A., Natawidjaja, D., McCaffrey, R., 2006. Plate-boundary deformation associated with the great Sumatra–Andaman earthquake. Nature 440, 46–51.

Taylor, F.W., Briggs, R.W., Frohlich, C., Brown, A., Hornbach, M.J., Papabatu, A.K., Meltzner, A., Billy, D., 2008. Rupture across arc segment and plate boundaries in the 1 April 2007 Solomons earthquake. Nat. Geosci. 1, 253–257.

Wallace, L.M., Barnes, P., Beavan, R.J., Van Dissen, R.J., Litchfield, N.J., Mountjoy, J., Langridge, R.M., Lamarche, G., Pondard, N., 2012. The kinematics of a transition from subduction to strike-slip: an example from the central New Zealand plate boundary. J. Geophys. Res. 117, B02405. http://dx.doi.org/10.1029/2011JB008640.